JOURNAL OF THERMOPHYSICS AND HEAT TRANSFER
Vol. 14, No. 2, April–June 2000

Multispectral Shock-Layer Radiance from a Hypersonic Slender Body

Deborah A. Levin*
George Washington University, Washington, D.C. 20052
Graham V. Candler†
University of Minnesota, Minneapolis, Minnesota 55455
and
Charles C. Limbaugh‡
Sverdrup Technology, Inc., Arnold Air Force Base, Tennessee 37388-9013

A methodology is presented for the calculation of the infrared (IR) shock-layer radiance from a slender hypersonic vehicle. An overlay technique that has been successfully employed for chemically reacting hypersonic compressed and expanding flows has been extended to model accurately the vibrational state distributions of NO, CO, water, and CO_2, which are potential shock-layer radiators in the midwave IR. The spectral predictions show that radiation from shock heated ambient CO_2 will be an important contribution at most altitudes and speeds slower than 3.5 km/s. A detailed vibrational state-specific model of CO_2 excitation has been incorporated with the flow modeling using an overlay technique. Comparisons of the spatial distributions of CO_2 vibrational states with a corresponding Boltzmann distribution at the translational temperature show that there are substantial differences in the populations. These predictions are important for the design of an upcoming sounding rocket experiment.

Nomenclature

A = Einstein spontaneous emission transition rate
h = Planck's constant
k = rate constant
u = flow velocities
$\hat{u}$ = diffusion velocities
w = chemical source function
x = flow directions
ν = frequency of light
ν_3 = CO_2 fundamental asymmetric stretching mode
ρ = mass density

Subscripts

i, l = CO_2 vibrational state index
j = flow direction index
s = overlay species index
v, v' = initial and final N_2 vibrational level

Introduction

THERE is a need to characterize and measure the UV radiation emitted by the flows about hypersonic vehicles. In addition to understanding the basic physics of high-temperature plasmas, ongoing analyses are establishing how such emissions are useful for the detection of theater missile targets using the midwave infrared (IR) spectral region (3–5 μm) as the baseline and the UV or visible wavelengths as a second detection wavelength.[1] The use of a second, shorter wavelength combined with the baseline sensor increases the total information content of the scene. Also, a two-color detection strategy based on both short and long wavelengths may provide robustness to the onboard seeker environment. This paper will present a methodology for the calculation of the self-induced, IR shock-layer radiance for a theater missile defense-like interceptor.

In support of these concepts, a sounding rocket experiment similar to the earlier bow-shock ultraviolet flight (BSUV) flights[2] is being planned. This experiment will fly the same trajectory as the BSUV 1 flight, that is, achieve a speed of 3.5 km/s by 40-km altitude, but will emphasize IR spectral measurements. The 4-in. nose radius of the BSUV 1 vehicle will be reduced to a value of less than 2 in. The calculations shown in this paper use the configuration of the proposed advanced interceptor technology (AIT) vehicle, which has a more slender forebody than that flown in the bow-shock flights. The use of an IR spectrometer, never before flown in such a configuration, will provide diagnostics of the shock-layer modeling complementary to our earlier work in the UV.[2,3] Earlier work in the UV emphasized the shock-layer modeling of NO and OH radiation,[3,4] species that potentially radiate in the IR spectral region 1.5–5.0 μm as well. The IR measurements should provide an assessment of the manner in which vibrational states are populated in the ground electronic state of these diatomic systems. In addition, IR transitions potentially will be seen from the polyatomic systems of water, carbon dioxide, and nitrogen dioxide. Based on our earlier research in UV radiation excitation mechanisms[5] and the anticipated collision rates, the baseline assumption is that the vibrational ground states are populated by collisions with the major species, N_2, at the translational temperature. However, this assumption will be examined here in more detail for the CO_2 system.

A key element in the flowfield modeling is the use of an overlay technique that we originally employed for a chemically reacting, hypersonic flow involving the dissociation of water to form OH (Ref. 4). This technique is important because it enables the inclusion of large numbers of chemical species and their reactions, as long as these species exist in trace quantities compared with the major flow species such as N_2, O_2, O, and NO. This is to be expected for the IR-active species such as water, its dissociated products, as well as carbon dioxide. Another facet of the computational efficiency of the overlay technique is that vibrational state-specific processes can be modeled for a large manifold of vibrational states by assuming each vibrational level to be a discrete species. This technique was employed in earlier work to model the neutral collisional excitation of a ladder of CO ground vibrational states to form an electronically excited state.[6] An extension of this technique is used in this paper

Received 26 July 1999; revision received 29 November 1999; accepted for publication 1 December 1999.

*Research Professor, Department of Chemistry. Member AIAA.
†Professor, Department of Aerospace Engineering and Mechanics and Army High Performance Computing Research Center. Member AIAA.
‡Senior Engineer, Arnold Engineering Development Center Division. Associate Fellow AIAA.

to model the state-specific population of CO_2 for a manifold of 28 vibrational states.

The outline of the paper is as follows. The following section discusses the thermochemical model used in the flow modeling of NO, NO_2, CO, CO_2, OH, and water, all of which are potential IR radiators. The calculations will show that there are insufficient collisions to assume thermochemical equilibrium. In the following section, the flow solutions are used to predict the IR spectra that would be seen at a side location aft on the body. A variety of freestream conditions were considered with altitude varied from 30 to 60 km and the speed varied by 2.5, 3.5, and 5.0 km/s. Although the experiment will be flown at a single speed, examination of the change of the spectral properties is instructive and will be discussed. Finally, the spectra predict the continued presence of CO_2 for the conditions of the flight experiment. Two state-specific models were used to test the assumption that the vibrational states are populated by the bulk translational temperature. The vibrational state-specific models and the comparisons of the population distributions with that of a Boltzmann distribution are presented for different conditions.

Thermochemical Model and Flow Calculations

The flow about the body can be modeled using an overlay method, which consists of two steps. First, the flowfield is simulated by solving the Navier–Stokes equations that have been extended to include the effects of finite-rate chemical reactions and internal energy relaxation. This solution includes all of the chemical species that may be present in large amounts or those that are important in the chemical kinetics of those major species. Then, the mass conservation equations for the trace chemical species are overlaid on the previously computed flowfield. Because the trace species are present in very small amounts, they do not affect the mass, momentum, or energy of the bulk flow. The computational fluid dynamics (CFD) method that was used to simulate the flow of the major species in the stagnation region of a reentry experiment[7] has been discussed in earlier work. The baseline model for air is a reacting mixture of thermally perfect gases composed of the following chemical species: N_2, O_2, NO, NO_2, N, and O. For the cases of interest here, they are considered to be the major species. These species are allowed to react with one another at finite rates. The internal energy is described by translational, rotational, and vibrational temperatures. Finite-rate relaxation of the rotational and vibrational temperatures to the translational temperature is also modeled. The thermochemical model used for the five species model of earlier work, N_2, O_2, NO, N, and O, remains the same. Table 1 gives the additional reactions that were introduced to model reactions involving NO_2.

Once the spatial profile of the air species (N_2, O_2, NO, NO_2, N, and O) has reached steady state, the chemical reactions involving the minor species of H_2O, OH, H, CO_2, C, and CO are considered. The reactions of these species were overlaid with the steady-state solution of the dry air species calculations in the following manner:

$$\frac{\partial \rho_s}{\partial x} + \frac{\partial(\rho_s u_j + \rho_s \hat{u}_{s,j})}{\partial u_j} = w_s$$

where s is the index for each of the overlay species, ρ_s is the mass density, w_s is the chemical source function, x_j are the flow directions (x and y), u_j are the flow velocities, and $\hat{u}_{s,j}$ is the diffusion velocity. The solution of this equation is much less costly than the solution of the full CFD for both bulk and overlay species because the cost varies approximately with the square of the number of equations being solved. This method successfully provides a full spatial solution of the trace species concentrations. The ability to account for diffusion of light species through the flow, such as H, is particularly important for the modeling of the water and OH chemistry. Ignoring such diffusion effects produces spatial profiles significantly different and incorrect. Hence, although the flow region of interest may be localized, a full spatial treatment is required. This factor will be even more significant for the calculation of IR radiation because the portion of the flow where the IR-active species is produced may be different than where the radiation occurs. As was done in earlier work, the argument is made that the introduction of the IR-active trace species in the flow cannot affect the energy or momentum of the bulk solution. Thus, a simplified conservation law for the expanded set of constituents (bulk plus overlay or trace) can be written that involves only the conservation of overlay species. Table 1 also lists the dissociation, exchange, and recombination processes that have been included in the overlay solution and the associated rate coefficients for these species.

Figure 1 shows the computational mesh used for an axisymmetric approximation to the AIT vehicle. The location of a side-viewing windows is also shown. Present planning for the sounding rocket experiment includes spectra to be obtained close to the stagnation point and at the side window. The same 100×100 point computational grid was used for all calculations shown in this work. The translational, vibrational, and rotational temperatures were computed for each freestream condition; however, for this altitude range there were sufficient collisions in the flow such that the translational and rotational temperatures were almost equal. The translational and vibrational temperatures, however, were not found to be equilibrated even at 40-km altitude. Figure 2 shows a comparison of the temperature contours at 40 km for the translational and vibrational temperatures. The translational temperature reaches a maximum of about 6000 K as compared with a maximum vibrational temperature of approximately 4500 K. As expected, the translational temperature

Table 1 Thermochemical model and rate coefficients[a]

Reaction	C_{fi}[b]	η_i	E_{fi}/R[c]	Third body, M
		Dissociation		
$H_2O + M \rightarrow OH + H + M$	3.5×10^{13}	0.0	50,584	N_2
$OH + M \rightarrow O + H + M$	7.5×10^{11}	0.06	50,563	N_2
$CO_2 + M \rightarrow CO + O + M$	6.9×10^{18}	−1.5	63,275	N_2, O_2, NO
	1.4×10^{19}	−1.5	63,275	N, O
$CO + M \rightarrow C + O + M$	2.3×10^{17}	−1	129,000	N_2, O_2, NO
	3.4×10^{17}	−1	129,000	N, O
		Exchange		
$O_2 + H \rightarrow O + OH$	2.2×10^{11}	0.0	8,377.5	——
$H_2O + O \rightarrow 2OH$	6.8×10^{10}	0.0	3,492.7	——
$CO + O \rightarrow O_2 + C$	3.9×10^{10}	−0.18	69,200	——
$CO_2 + O \rightarrow O_2 + CO$	2.1×10^{10}	0.0	27,800	——
$N + NO_2 \rightarrow 2NO$	2.41×10^{9}	0.0	−500	——
$NO_2 + O \rightarrow NO + O_2$	1.02×10^{10}	0.0	−300	——
		Recombination		
$NO + O + O_2 \rightarrow NO_2 + O_2$	1.45×10^{9}	0.0	900	——
$NO + O + N_2 \rightarrow NO_2 + N_2$	2.03×10^{9}	0.0	900	——
$2NO + O_2 \rightarrow 2NO_2$	1.2×10^{3}	0.0	530	——

[a]Rate coefficient is $C_{fi} T_i^{\eta} \exp(-E_{fi}/T)$. [b]Rates are in cubic centimeter per mole per second or higher.
[c]$R = 1.98$ cal/mole-K; E_{fi} is in calories.

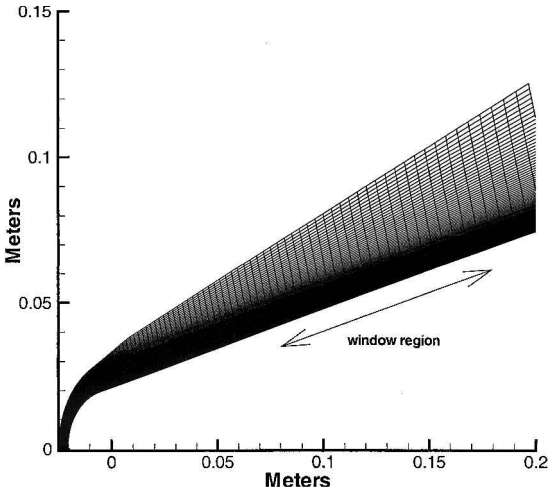

Fig. 1 Computational mesh of AIT vehicle.

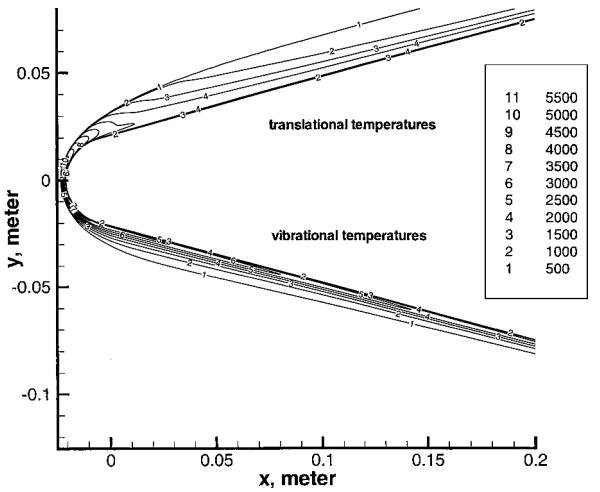

Fig. 2 Comparison of translational temperature contours (top) with vibrational temperature contours (bottom) at 40-km altitude, 3.5 km/s.

is much lower in the region of the side-mounted window than at the stagnation point, but still higher than the vibrational temperature. At 50 and 60 km the degree of thermal nonequilibrium increases, and the difference in the spatial distribution of the translational and vibrational temperatures is more pronounced.

The two sources of IR shock-layer radiation are from molecules that are present in the atmosphere and those that are formed in the bow-shock chemistry. Molecules such as CO_2 and H_2O that are present in the atmosphere in trace quantities[8,9] can provide a large source of IR radiance when they are heated in the shock layer. Bow-shock chemistry produces NO and NO_2 from the major atmospheric species of N_2 and O_2, as well as OH from the dissociation of water. (Only small amounts of CO_2 dissociation to CO + O is predicted.) The relative importance of the two types of formation processes will be determined by the collision rates. Hence, the spectra should change as a function of altitude because the dominant molecular radiators change from those formed by shock-layer chemical reactions (low altitudes) to that favored by the heating of the ambient atmospheric species. Table 2 gives the freestream conditions that were used in this work. Figure 3 shows a comparison of the number density profiles of NO and OH at 40-km altitude, 3.5 km/s along the stagnation streamline and at the side-window location. The spatial variability of CO_2 and water (not shown) is much less than that of NO or OH. Nitric oxide is formed in the stagnation region at a maximum quantity of about 10^{17} number/cm^3. However, at the aft location the spatial extent of the NO number density is comparable to the CO_2 number density, which is has a relatively constant concentration in the shock layer between 10^{14} and 10^{15} number/cm^3.

Table 2 Atmospheric conditions

Altitude, km	Number density, number/cm^3	Water mixing ratio	CO_2 mixing ratio
30	3.69*e*17	1.6*e*−5	3.4*e*−4
40	8.26*e*16	1.6*e*−5	3.4*e*−4
50	2.19*e*16	1.6*e*−5	3.4*e*−4
60	6.67*e*15	1.5*e*−5	3.4*e*−4

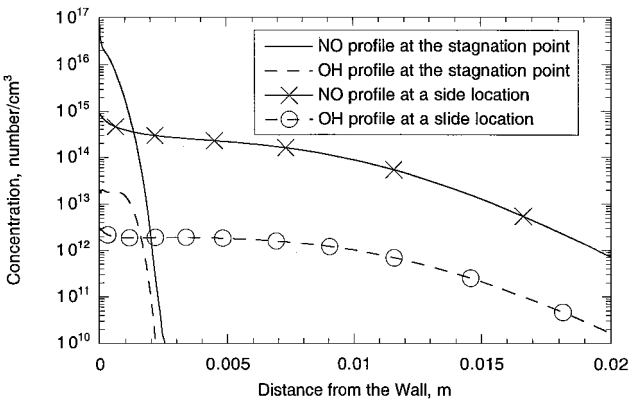

Fig. 3 NO and OH number density profiles at the stagnation streamline and at the side-window location at 40-km altitude, 3.5 km/s.

In fact, comparison of the relative NO and CO_2 concentrations at higher altitudes (for the same speed) showed that only at 40 km and in the stagnation region is the NO concentration significantly higher than that of CO_2. In a manner similar to that of CO_2, the water has an almost constant distribution about the body with a concentration of $\sim 10^{11}$–10^{12} number/cm^3. In contrast to water, Fig. 3 shows that the spatial distribution of OH is nonuniform, and its maximum concentration is in the stagnation region where there is the greatest amount of water dissociation. However, the amount of water dissociation is low; thus, we would expect a small spectral contribution from OH.

IR Spectral Shock-Layer Calculations

Through the use of the translational temperature and species distributions, the IR spectra were computed using the ATHENA[10] radiative transport band model. A spectral resolution of 25 cm^{-1} was used because that is the anticipated spectral bandwidth of the onboard spectrometer. Spectra shown here are calculated at each grid point along a line of sight normal to the body in the side-viewing window region shown in Fig. 1. Hence, the spectra represent an integration over the nonconstant temperatures and concentrations along the line of sight. Figure 4 shows the spectra from 1.5 to 5 μm at 3.5 km/s, 40-km altitude. The spectrometer will measure the composite spectra, but for the purpose of analyzing the spectra, the separate molecular components are shown. It can be seen that the dominant radiator for these conditions is CO_2 and then water. This is consistent with the flowfield species distributions discussed earlier.

The calculations of Trolier et al.[11] suggest that NO_2 could contribute to the spectra in the region between about 3.5 and 4 μm. Figure 4 shows that we predict a small amount of NO_2 radiation and is consistent with our flow chemistry modeling, which predicts orders of magnitude less NO_2 concentration than NO. The main production mechanism for NO_2 was found to be the reverse process of the sixth exchange reaction given in Table 1.

Although the experiment to be flown will collect spectra for a sounding rocket flying at a constant speed of 3.5 km/s (vertically), it is interesting to compare the spectra given in Fig. 4 with that predicted for a flight at 5 km/s and 40-km altitude. Figure 5 shows the predicted spectra at the higher speed. Consistent with the thermochemical model, the higher speed, that is, higher translational temperature, increases the chemical reaction rates to produce more NO and NO_2. Figure 6 shows the total spectra at an altitude of 30 km for three different speeds. Again, as the collision rates increase (higher speeds), the species that are produced by the

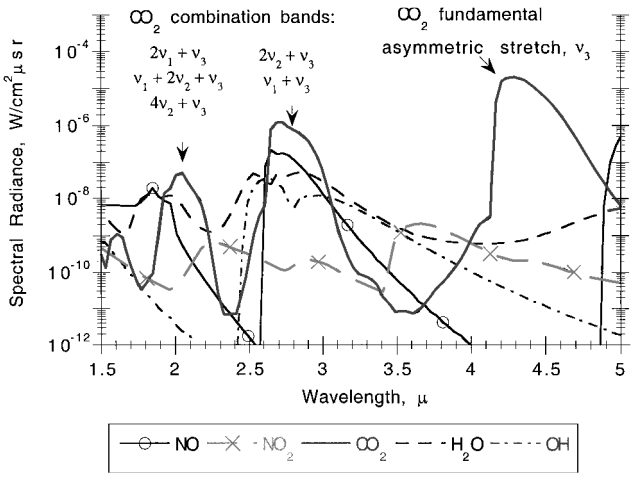

Fig. 4 Calculated spectra at 40-km altitude, 3.5 km/s.

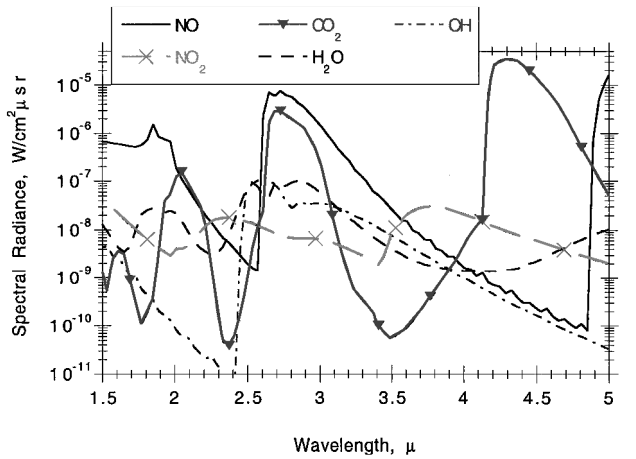

Fig. 5 Calculated spectra at 40-km altitude, 5.0 km/s.

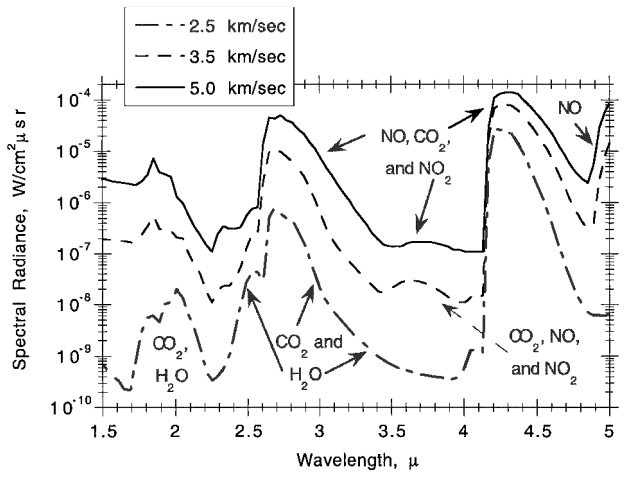

Fig. 6 Comparison of calculated spectra at 30-km altitude for different speeds.

shock-layer chemistry contribute more to the spectra. At lower speeds, the opposite is seen (see the curve at 2.5 km/s) for a fixed speed, the shock-layer kinetics will also vary at different altitudes, and the NO and NO_2 features will be more evident at lower altitudes.

Carbon Dioxide Vibrational State Modeling

State-specific modeling can potentially impact the modeling of the IR shock-layer radiance. The thermal nonequilibrium aspect of the flow as shown earlier is an indication that vibrational state-specific modeling may be important. The calculated spectra of Fig. 4 are integrated over a slice of gas along a line of sight normal to the vehicle surface with a temperature of about 2500 K. However, the temperature at the stagnation point is approximately 6000 K, and the vibrational distribution of the radiating species created at the stagnation point can be different than that aft on the body. If the overall deexcitation rate processes are on the order of the gas velocity, then the enhanced populations created at the stagnation point, relative to those downstream, will generate spectra different in magnitude and shape from those shown in Fig. 4. A similar concept was explored by Sundberg et al.[12] in their modeling of nonequilibrium IR emission from reentry wake flows. Their work considered many of the important energy exchange processes for the species of interest here, namely, $V-T$ and $V-V$ transfer for CO_2 with flow species such as N_2, O_2, and O. However, their work did not integrate the exchange processes with a thermochemical hypersonic treatment of the flow and was applied only to the wake flow.

Since the spectra were shown to be dominated by CO_2 radiation, we have chosen that species as a candidate for understanding vibrational nonequilibrium of an IR radiator. Figure 4 shows the spectra of CO_2 at 3.5 km/s, 40-km altitude with the prominent CO_2 spectral features and specific transitions identified. The number of vibrational modes and nomenclature is more complex for CO_2, a polyatomic system, than a diatomic system; however, vibrational spectra have been extensively studied and characterized for CO_2 (Refs. 13 and 14). In the spectral region of interest here, the fundamental asymmetric stretching mode ν_3 radiates at 4.3 μm. Additional transitions from the combination bands (transitions between summation of fundamental mode states and the ground state) contribute to the total CO_2 spectra.

In earlier work we used the overlay method to solve for the full spatial solution of a manifold of the ground vibrational states of CO and the electronically excited CO(a) state in an expanding flow.[6] This work has been further developed to consider the vibrational transitions in the polyatomic CO_2 system. Two vibrational models were considered in this work with the salient features, that is, the types of excitation processes included and the number of states, outlined next.

The first vibrational state-specific model considers the following types of processes:

$$CO_2(l) \xrightarrow{A_{li}} CO_2(i) + h\nu$$

$$CO_2(l) + M \xleftrightarrow{k_{li}} CO_2(i) + M$$

$$CO_2(l) + N_2(v=0) \xleftrightarrow{k_{li}^{vv'}} CO_2(i) + N_2(v'=1)$$

where the first process represents spontaneous emission, the second process involves $V-T$ collisions with a third body, $M = N_2$, O_2, and O, and the last expression represents a $V-V$ process. The rates are taken from the work of Taylor and Bitterman[15] and Sundberg et al.[12] As is pointed out by Sundberg et al., the $V-V$ process with N_2 is a near-resonant process and is potentially a major contributor to the excitation of the ν_3 fundamental mode and the combination bands. We have included 28 vibrational states (see Fig. 7 of Sundberg et al.[12]), which includes states up to levels of approximately 5000 cm^{-1} of energy.

The maximum energy level chosen in the Sundberg et al.[12] model was appropriate to the calculation of radiation from a reentry wake flow that is predicted to have lower temperatures than would be obtained in the bow-shock region. To test the sensitivity of our results to the maximum energy level cutoff, we could expand the ladder of CO_2 vibrational states. This, however, would significantly increase the number of vibrational states. Limbaugh and Drakes[16] and Limbaugh et al.[17] have considered this complexity and proposed a physically realistic solution. This approach, which will be outlined subsequently, permits us to increase the ladder of CO_2 vibrational states, yet maintain the same types of $V-V$ processes as was included before. Figure 4 of Ref. 16 shows the energy-level diagram and definition of states. In contrast to the earlier model of Sundberg

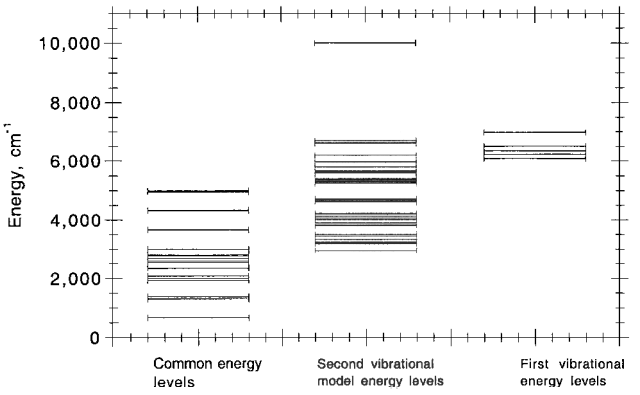

Fig. 7 Comparison of CO_2 vibrational levels in the two vibrational state models considered.

et al.,[12] the ladder of states extends up to energies of 10,000 cm^{-1}. High-energy levels, which may be assumed to be in thermal equilibrium, are grouped into single super states. Super states are defined for $v_3 = 0$ to include all states between 5800 and 10,000 cm^{-1}, for $v_3 = 1$ to include all states between 6200 and 10,000 cm^{-1}, and for $v_3 = 2$ to include all states between 6700–10,000 cm^{-1}. The inclusion of high-energy states provides a reservoir that is necessary to ensure completeness (or results that are independent of the upper state cutoff). States with the fundamental vibrational mode quantum numbers v_i for $i = 1, 2, 3$ with maximum values of 4, 8, and 2, respectively, are included in the model. The accidental degeneracy or Fermi resonance present in the CO_2 system expands the usual vibrational state definition from three to five quantum numbers.[14] However, it is not necessary to represent each specific state implied by the five quantum numbers. Instead states that exhibit the Fermi resonance and close energy coupling are assumed to be in local thermodynamic equilibrium and are grouped together as a single state.[16,17] Figure 7 shows a comparison of the energy levels in the two vibrational models. Most of the lower energy levels are common to both models; however, it can be seen that the second model contains many states between 3000 and 6000 cm^{-1} energy.

The second vibrational state-specific model considers processes similar to the first. Radiative decay between vibrational states is not included; however, these were found to have no impact on the kinetics solutions of the first model. Similar to the first model, $V - T$ and $V - V$ rates are included, and for the latter transitions the reaction set is expanded from the $N_2(v = 0)$, $N_2(v = 1)$ states to include specific vibrational states of CO_2. The $V - T$ and $V - V$ rates are taken from a review by Blauer and Nickerson.[18]

The flow solution for the spatial distribution of each of the vibrational states for the two vibrational models provides a large amount of computational data to examine and analyze, at each specific altitude considered. All calculations were performed for a speed of 3.5 km/s, for altitudes of 30, 40, 50, and 60 km, and the freestream mixing ratio for CO_2 given in Table 2. Results will be presented and discussed at four flow conditions that represent the maximum differences expected for this range of parameters. Table 3 summarizes the flow parameters at these four locations and flight conditions.

First consider the time-dependent solutions of the two models at a constant temperature and number density corresponding to a flow condition. Figures 8 and 9 show the solutions for three vibrational states corresponding to the 4.3, 2.7, and 2.0 μm transitions at conditions corresponding to 30-km altitude in the stagnation region and 60-km altitude along the side of the body. These calculations represent limiting conditions where steady state is quickly reached in the flowfield vs a condition where the flow residence time is short compared to the time to populate the CO_2 vibrational levels. Indeed both kinetic models predict a time constant to reach steady state on the order of 10^{-6} s for Fig. 8 vs 10^{-4} s for Fig. 9. Note that in both cases the steady-state limit of the three vibrational state populations is significantly lower for the first vibrational model than the second. At the 30-km altitude condition, the first vibrational model requires significantly more time to reach steady state than the first. At 60-km altitude there is little difference in the time constants of the two kinetic solutions.

Table 3 CO_2 state-specific vibrational model conditions for four flow points

Case	Total number density, number/cm^3	Translational temperature, K	Vibrational temperature, K
30 km, stagnation region	2.27×10^{18}	5639	2357
30 km, aft/window region	4.18×10^{17}	2274	2567
60 km, stagnation region	2.56×10^{16}	6777	874
60 km, aft/window region	8.28×10^{15}	2099	732

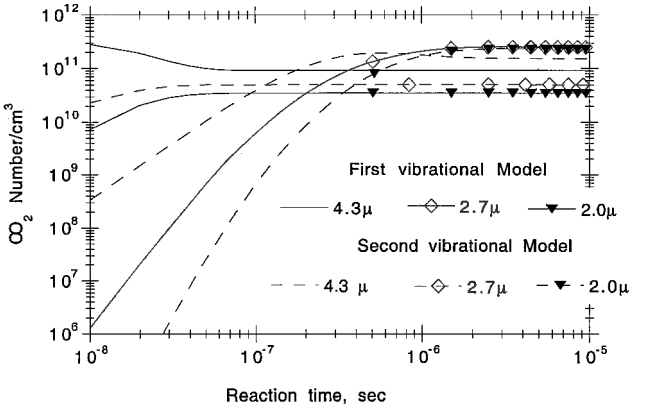

Fig. 8 Comparison of kinetic rate equation solutions for the two vibrational models at 3.5 km/s, 30-km altitude at the stagnation point.

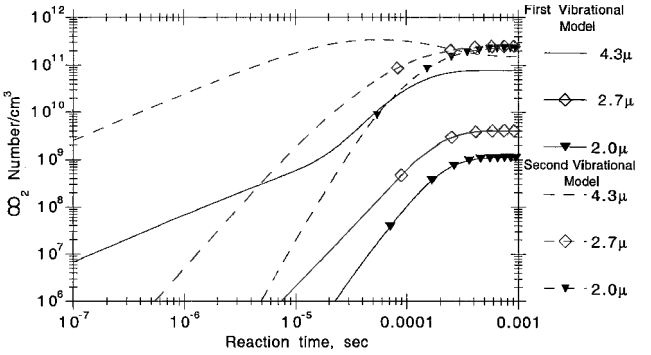

Fig. 9 Comparison of kinetic rate equation solutions for the two vibrational models at 3.5 km/s, 60-km altitude at the side location.

Figures 10–13 show the CO_2 vibrational state populations predicted by the solution of the continuum flow equations at the four locations and freestream flow conditions given in Table 3. The population of each level divided by its degeneracy is plotted as a function of the energy level to enable comparisons with a Boltzmann distribution at the gas translational temperatures given in Table 3. For three of the four cases, the first vibrational model predicts a population distribution significantly different than a Boltzmann distribution. As in the single point kinetic analyses, the first vibrational model has a lower population than that of the second. Although the lower energy vibrational states can be seen to overpopulate (relative to a Boltzmann distribution), they do not radiate in the spectral region of interest. Moreover, the three states of interest are seen in those three cases to be significantly lower than a Boltzmann distribution. The spectral peaks shown in Fig. 4 would be reduced by the corresponding ratio of the population predicted by the first vibrational model to that of a Boltzmann distribution. Figures 10 and 11 show that the second model predicts a distribution very close to that of a Boltzmann distribution, as would appear reasonable at 30-km altitude. At 60-km altitude, Figs. 12 and 13 show that both models predict distributions significantly different from that of a

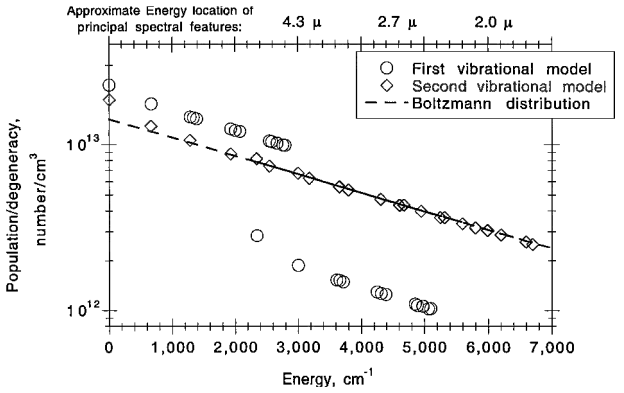

Fig. 10 Comparison of predicted CO_2 vibrational populations at 3.5 km/s, 30-km altitude at the stagnation point.

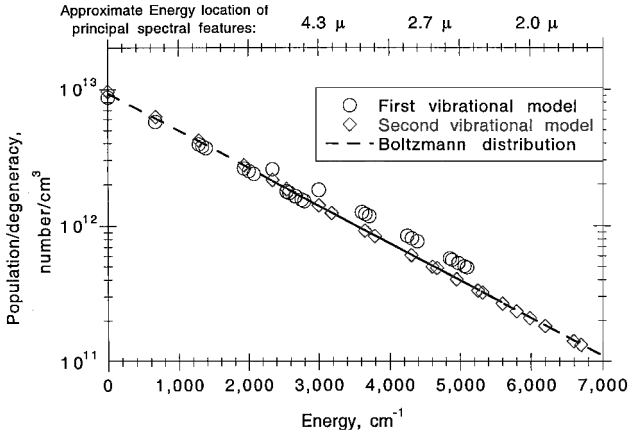

Fig. 11 Comparison of predicted CO_2 vibrational populations at 3.5 km/s, 30-km altitude at the side location.

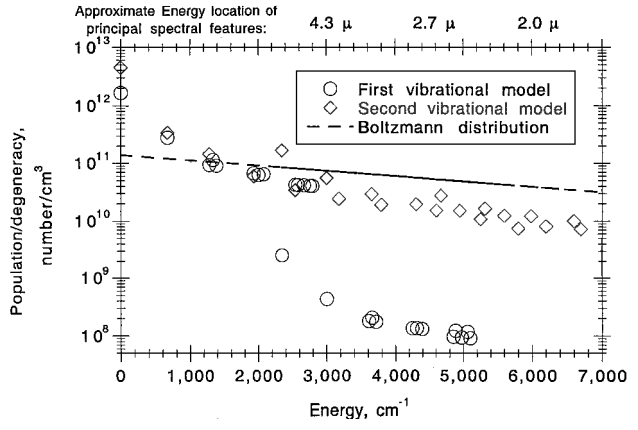

Fig. 12 Comparison of predicted CO_2 vibrational populations at 3.5 km/s, 60-km altitude at the stagnation point.

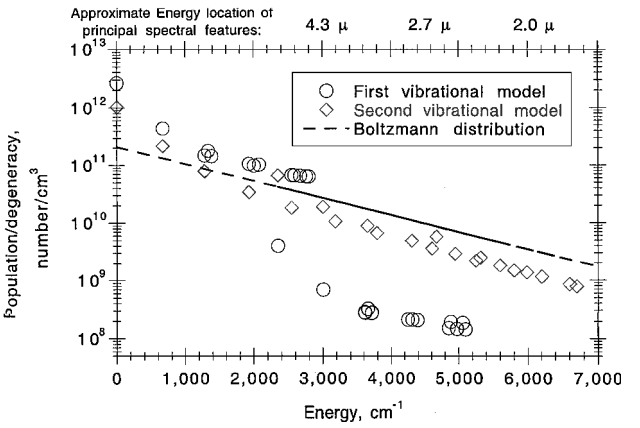

Fig. 13 Comparison of predicted CO_2 vibrational populations at 3.5 km/s, 60-km altitude at the side location.

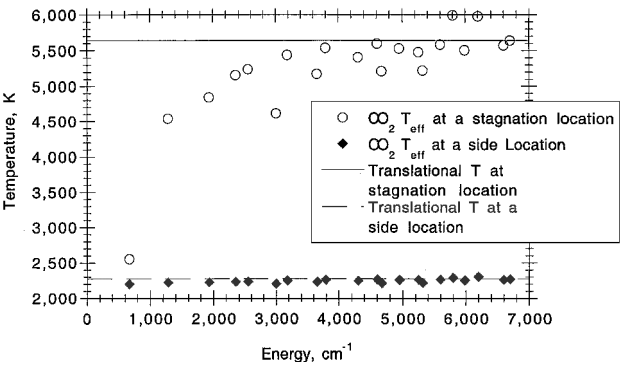

Fig. 14 Comparison of effective CO_2 vibrational temperatures at 3.5 km/s, 30-km altitude using the second vibrational state model with the gas temperature.

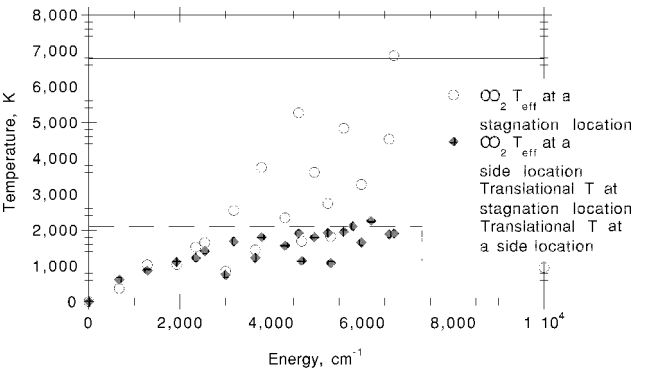

Fig. 15 Comparison of effective CO_2 vibrational temperatures at 35 km/s, 60-km altitude using the second vibrational state model with the gas temperature.

Boltzmann distribution. Again, however, the second model predicts a much smaller deviation than the first. In general, the second vibrational model appears to give a more reasonable prediction. The large deviation from a Boltzmann distribution of the first vibrational model seen in Fig. 10 is probably due to an insufficient number of vibrational states between 3000 and 6000 cm^{-1} (see also Fig. 7).

Because the second vibrational model predicts a distribution of states clustered about the Boltzmann distribution, it is reasonable to calculate the effective temperature implied by ratio of adjacent vibrational levels. Figures 14 and 15 show a comparison of the effective temperature for each vibrational state at the four conditions considered earlier with the gas translational temperature. At 30-km altitude the effective temperatures are essentially the gas translational temperature at the side location. At the stagnation point there is no single value for the effective temperature, but the individual values approach the corresponding gas translational temperature. At 60 km the deviation between the effective temperatures and the gas temperature is larger at both locations, as would be expected from Figs. 12 and 13. Moreover, it is not possible to define a single effective temperature for the 60-km, condition.

Conclusions

We have discussed a method to calculate the spatial distribution of IR radiating species in a hypersonic shock layer. The baseline model for excitation of ground vibrational states by collisions with N_2 at the translational temperature has been used in a spectral band

model to predict the bow shock IR spectra. At a speed of 3.5 km/s, radiation from the ambient CO_2 heated in the shock layer was found to be the major contribution between the altitudes of 30 and 60 km. Hence, a detailed vibrational state treatment to model the population of the ground vibrational states of that species was examined. Using a modification of the overlay technique developed to obtain solutions of the spatial distribution in the shock layer of large numbers of radiating trace species, we observed large differences between the baseline excitation model (a Boltzmann distribution at the translational temperature) and the first vibrational state model. The second vibrational model did not exhibit as large a difference with the baseline excitation model, and in some cases the effective temperature approaches the gas translational temperature. However, the results of the comparison show that for both vibrational models there is a departure from the baseline model for these flow conditions. If the inclusion of more vibrational levels at higher energies gives a distribution closer to that of the Boltzmann distribution, it is likely that the second model gives a better representation of the flow conditions. Ultimately comparison of spectra obtained from an upcoming flight experiment will determine which is the better of the two excitation models.

Acknowledgments

The work at George Washington University was supported by Army Research Office Grant DAAG55-98-1-009 and at University of Minnesota by Army Research Office Grant DA/DAAG55-97-1-0406. Computer time was provided by the University of Minnesota Supercomputer Institute. This work is also sponsored in part by the Army High Performance Computing Research Center under the auspices of the Department of the Army, Army Research Laboratory Cooperative Agreement DAAH04-95-2-0003/Contract DAAH04-95-C0008.

References

[1]Levin, D., Caveny, L., Beaghler, G., and McDermott, P., "Dual-Mode Spectral Detection of Hypersonic Flows," *The International Society for Optical Engineering, SPIE, 10th Meeting on Optical Engineering in Israel*, Vol. 3110, 1997, pp. 141–150.

[2]Erdman, P. W., Zipf, E. C., Espy, P., Howlett, C., Levin, D. A., Loda, R., Collins, R. J., and Candler, G. V., "Flight Measurements of Low-Velocity Bow Shock Ultraviolet Radiation," *Journal of Thermophysics and Heat Transfer*, Vol. 7, No. 1, 1993, pp. 37–41.

[3]Levin, D. A., Candler, G. V., Collins, R. J., Erdman, P. W., Zipf, E., Espy, P., and Howlett, C., "Comparison of Theory with Experiment for the Bow Shock Ultraviolet Rocket Flight," *Journal of Thermophysics and Heat Transfer*, Vol. 7, No. 1, 1993, pp. 30–36.

[4]Levin, D., Collins, R., Candler, G., Wright, M., and Erdman, P., "Examination of OH Ultraviolet Radiation from Shock-Heated Air," *Journal of Thermophysics and Heat Transfer*, Vol. 10, No. 2, 1996, pp. 200–208.

[5]Levin, D., Candler, G., Collins, R., Erdman, P., Zipf, E., and Howlett, C., "Examination of Theory for the Bow Shock Ultraviolet Rocket Experiments—I," *Journal of Thermophysics and Heat Transfer*, Vol. 8, No. 3, 1994, pp. 447–452.

[6]Levin, D., Candler, G., and Collins, R., "An Overlay Method for Calculating Excited State Species Properties in Hypersonic Flows," *AIAA Journal*, Vol. 35, No. 2, 1997, pp. 288–294.

[7]MacCormack, R. W., and Candler, G. V., "The Computation of Hypersonic Ionized Flows in Chemical and Thermal Nonequilibrium," *Journal of Thermophysics and Heat Transfer*, Vol. 5, No. 3, 1991, pp. 266–273.

[8]Jurda, A. S., *Handbook of Geophysics and the Space Environment*, U.S. Air Force, 1985.

[9]Brasseur, G., and Solomon, S., *Aeronomy of the Middle Atmosphere*, 2nd ed., D. Reidel, Dordrecht, The Netherlands, 1984.

[10]Devore, J., "ATHENA User's Guide," TM, Photon Research, Inc., Sept. 1987.

[11]Trolier, J., Hudson, D., Carlson, D., and Krawczyk, W., "Shocklayer Radiance Effects on Endoatmospheric Interceptor Seeker Performance," AIAA Paper 92-2816, May 1992.

[12]Sundberg, R. L., Duff, J. W., and Bernstein, L. S., "Nonequilibrium Infrared Emission Model for the Wake Flow of Reentry Vehicles," *Journal of Spacecraft and Rockets*, Vol. 30, No. 6, 1993, pp. 731–741.

[13]Herzberg, G., *Molecular Spectra II Infrared and Raman Spectra of Polyatomic Molecules*, D. Van Nostrand, New York, 1945.

[14]Rothman, L., Gamache, R., Goldman, A., Brown, L., Toth, R., Pickett, H., Poynter, R., Flaud, J., Camy-Peyret, C., Barbe, A., Husson, N., Rinsland, C., and Smith, M., "The HITRAN Database: 1986 Edition," *Applied Optics*, Vol. 26, No. 19, 1987, pp. 4058–4097.

[15]Taylor, R. L., and Bitterman, S., "Survey of Vibrational Relaxation Data for Processes Important in the CO_2–N_2 Laser System," *Review of Modern Physics*, Vol. 41, No. 1, 1969, pp. 26–47.

[16]Limbaugh, C. C., and Drakes, J. A., "CO_2 Vibrational Relaxation Effects in a Laser-Heated Hypersonic Flow," AIAA Paper 97-2492, June 1997.

[17]Limbaugh, C. C., Tramel, R. W., Drakes, J. A., and Hiers, R. S., III, "Analysis of CO_2 Vibronic Ensembles in Nonequilibrium Combustion Flows," AIAA Paper 94-1985, June 1994.

[18]Blauer, J. A., and Nickerson, G. R., "A Survey of Vibrational Relaxation Rate Data for Processes Important to CO_2–N_2–H_2O Infrared Plume Radiation," AFRPL-TR-73-57, U.S. Air Force Rocket Propulsion Lab., Oct. 1973.